Durability indicators of slag-based concrete reinforced by steel fibers: experimental study and multiscale modeling

Nicolas Reuge, Stéphanie Bonnet, François Bignonnet

Durability indicators of slag-based concrete reinforced by steel fibers: experimental study and multiscale modeling

Nicolas Reuge[1,*], Stéphanie Bonnet[1] and François Bignonnet[1]

[1]Nantes Université, Ecole Centrale Nantes, CNRS, GeM, UMR 6183 F-44600, Saint-Nazaire, France

[*]Corresponding author, email: reuge@free.fr

Abstract

This study is part of a project investigating the possible use of slag-based concretes reinforced by steel fibers for various structures of critical interest, exposed to marine environments and aimed at improving the characteristics of the structure compared to the classical solution of plain reinforced concretes. Four concrete mix designs were investigated featuring various fiber contents: 0 $kg.m^{-3}$ (i.e., without fiber), 20 $kg.m^{-3}$, 40 $kg.m^{-3}$ and 60 $kg.m^{-3}$. Mechanical properties and durability indicators were tested, focusing on chloride diffusivity (migration tests) and electrical resistivity (Wenner tests). Migration tests showed that chloride diffusivity increases moderately between 0 $kg.m^{-3}$ and 40 $kg.m^{-3}$ fiber content (25%) and more strongly between 40 $kg.m^{-3}$ and 60 $kg.m^{-3}$ fiber content (21%). With regard to mechanical properties, the best compromise for fiber content is 40 $kg.m^{-3}$. Thanks to a multiscale homogenization model coupled with a hydration model, the effect of fibers on the durability indicators is determined. It successfully reproduces the increases in resistivities as a function of time and their decreases as a function of fiber content. The moderate increase in chloride diffusivity with fiber content (≤ 40 $kg.m^{-3}$) is also well reproduced by accounting for an interphase of 22 µm width around the fibers.

keywords: steel fiber-reinforced concrete, blast furnace slag, durability, chloride, corrosion, multiscale homogenization model

1 Introduction

In marine environments, Reinforced Concrete (RC) structures are subjected to sea water penetration and chloride ingress (Lu et al. 2015). When chloride ions reach the steel rebars in sufficient quantities, corrosion initiates, ultimately leading to catastrophic cracking of the matrix and drastic loss of mechanical properties of the structure.

It is now well established that replacing part of the cement by Blast-Furnace Slag (BFS) in the concrete mix design modifies the matrix of the porous network (Fabien et al. 2022) in a highly efficient way, slowing down chloride ingress (Ben Fraj et al. 2012; El Achrafi et al. 2023). Moreover, BFS is significantly less impactful on the environment than clinker (Ventura et al. 2020).

Another possibility for increasing the service life of RC could consist in adding steel fibers in the concrete mix design (Ali et al. 2023). The corrosion resistance of Steel Fiber-Reinforced Concretes (SFRC) is not a priori obvious since steel fibers can also be subjected to corrosion. However, SFRC have better corrosion resistance than RC, which is attributed to the formation of a macro-cell circuit by fibers in concrete (Ren et al. 2024). The macro-cell inhibits the corrosion of the internal reinforcement due to cathodic protection. From (Song et al. 2023), the corrosion process of fibers differs as a function of the fiber content: at less than 2 vol%, it initiates at fibers edges through matrix defects whereas at more than 2 vol%, through a well-connected conductive network, it can initiate at fibers centers under the action of spontaneous current and macro-cell reaction.

Furthermore, it is established that the introduction of steel fibers in concrete mix designs results in significant gains in mechanical properties (Ali et al. 2023, Thomas and Ramaswamy 2007) possibly enabling the rebars to be dispensed with. In this study, double-hooked steel fibers were used: they are known to be particularly interesting to provide good ductility to the concrete (Rezakhani et al. 2021).

Figure 1 shows an overview of the project focused on Steel-Fiber Reinforced Slag-Based Concretes (SFRSBCs). The aim of the entire project is twofold: (1) determining the optimal content of steel fibers and (2) obtaining a favorable Life Cycle Assessment (LCA). The present investigations deal with the

first point only. The optimal content of fibers should provide a maximized durability of the structure with regards to chloride ingress together with suitable mechanical properties. Investigating durability as a function of the mix design requires: (a) measurements of durability indicators; (b) linking modifications of these indicators to the material microstructure which can be done by using multiscale homogenization techniques.

Figure 1

Many studies investigating the effects of steel fibers on mass transport in SFRCs focus on liquid permeability. Although there is no universal relationship between liquid permeability and chloride diffusivity, they usually follow the same trends. In (Poorsaheli et al. 2021), all the SFRCs tested (fiber volume fraction between 0.33% and 0.99%) had a lower water permeability (from 50% to 80%) compared to the plain concrete samples. Previous studies have stated that the presence of fibers reduces crack initiation and propagation in the concrete (Tsukamoto and Wörner 1991; Lawer et al. 2002; Rapoport et al., 2002), resulting in lower permeability.

From the review by Ganesh and Sofi (2022) and from various investigations (Benmokrane et al. 1996; Kamal and Boulfiza 2011; Pakravan et. al. 2017; Stefanoni et al., 2015; Poorsaheli et al. 2021; Farooq and Yokota 2022; Yang et al., 2022; Zhang et al., 2022) and on-site measurements (Ganesh and Sofi 2022), it seems that the presence of steel fibers in concretes can reduce chloride ingress.

However, in the measurements performed by Ortega-Lopez et al. (2022), the use of steel fibers (volume fraction of 0.5%) slightly worsened the durability behavior of the studied SFRC, facilitating chloride ingress. Two studies (Shin et al. 2020; Fattouh et al. 2023) found that the addition of steel fibers degraded the durability of SFRCs in corrosive environments, especially when the concrete cracks despite an initial beneficial effect of restricting the water penetration depth. The Rapid Chloride Migration Tests (RCMTs) performed in (Zhao et al. 2023) showed that steel fibers may cause accelerated chloride ion penetration for a fiber volume fraction greater than or equal to 0.8%. Therefore, it appears that the effect of steel fibers on chloride ingress in SRFCs is a very controversial topic.

To our knowledge, SFRSBCs have never been studied except by Kim et al. (2021). Their RCMTs showed that adding fibers led to a significant decrease in chloride diffusivity.

Alternatively, concrete resistivity is a property which can be easily measured. It is particularly sensitive to liquid water content which has a low electric resistance. During the process of hydration, water content decreases and resistivity increases. Obviously, in SFRCs, resistivity also depends on steel fiber content.

Multiscale modeling can provide understanding on the effect of the composition and microstructure of SFRCs on their diffusive and resistive properties evolution during hydration. These models rely on a geometrical description of the microstructure and material properties at several length scales. For example, the mechanical properties of SFRCs have successfully been modeled using continuum micromechanics (Sorelli et al. 2008, Qsymah et al. 2017, Chen et al. 2020, Yu et al. 2020, Li et al. 2024). Shen et al. (2023, 2024) modeled the water permeability of hybrid fiber reinforced concrete using the General Effective Media Theory with a three-scale microstructure description. Both the electrical resistivity and diffusion coefficient of concrete can also be modelled using multiscale homogenization methods and hydration models (Béjaoui et al. 2006, Stora et al. 2008, Damrongwiriyanupap et al. 2017; Achour et al. 2020; Honorio et al. 2020). Yet, to the best of our knowledge, the diffusivity and electrical resistivity of SFRCs has not been modeled using multiscale methods. According to the Nernst-Planck equation, the electrical resistivity and diffusion coefficient of plain concrete are closely related (Baroghel-Bouny et al. 2011; Chidiac and Shafikhani 2020). Hence, a multiscale model validated on resistivity measurements could be used to model the diffusion coefficient.

First, the SFRSBC mix designs are detailed and the measurement methods are described: RCMTs and resistivity measurements. Results are presented as a function of time and fiber content and compared to values found in the literature. Beside this, samples are characterized mechanically. Then, a multiscale model of SFRBCs is developed based on mean-field homogenization methods. The evolution of microstructure and of macroscopic properties of the material will be accounted for by an

existing hydration model in combination with a homogenization model. In terms of durability indicators, results are finally compared with measurements.

2 Materials and methods

2.1 Concrete mix design and fabrication

The base mix design of the reference concrete is given in Table 1. The binder is composed of 50% CEM I cement (Ordinary Portland Cement, OPC) and 50% BFS provided by Ecocem™. Sand and gravels are provided by Groupe CB™ (Boulonnais quarry). Water to binder mass ratio is 0.48. The physical and chemical properties of OPC and BFS are given in Tables 2 and 3 respectively.

The chosen steel fiber is Dramix 5D from Bekaert™ (Figure 2). The physical properties of this double-hooked fiber (0.9 mm diameter, 63 mm length) are given in Table 4.

Figure 2

Tables 1–4

As shown in Table 5, from the base formulation, four mix designs were produced: F0, F20, F40 and F60 with fiber contents of 0 $kg.m^{-3}$, 20 $kg.m^{-3}$, 40 $kg.m^{-3}$ and 60 $kg.m^{-3}$ respectively. To ensure sufficient and similar workability of the fresh concretes, a polycarboxylate-based superplasticizer (Master-Glenium 201 BASF™) was added, from 2.37 $kg.m^{-3}$ for F0 to 3.95 $kg.m^{-3}$ for F60 (Table 5). These mix designs were validated by our industrial partner Charier™ and by Bekaert™.

Table 5

From every mix design, 13 cylindrical concrete specimens, 11 cm diameter and 22 cm height, were produced.

2.2 Water porosity and compressive strength at day 28

After 28 days of moist cure, some specimens were cut in slices of 5 cm height. Eight cylindrical slices (2 per mix design), were weighed and dried in an oven at a temperature of 60 °C, a temperature that preserves the microstructural integrity of the concrete. After 5 months of drying, stabilization of the sample masses indicated complete evaporation of the water initially present in the open porosity φ.

Thus, values of φ were deduced: whatever the mix design, they were in the range of 11.1%±0.5, as shown in Table 6.

Table 6

2.3 Rapid Chloride Migration Test (RCMT)

The determination of chloride diffusivity in concretes in natural conditions is extremely long. Hence, the technique of RCMT was used, standardized as NT Build 492 (1999) and XP P18-462 v2 (2017): after the curing period, concrete samples were sawn into 50 mm thick cylindrical slices. The slice was placed between the two compartments of a migration cell. The downstream compartment contains a basic solution (NaOH: 3 g.l^{-1}); the same solution is laden with NaCl (35 g.l^{-1}) in the upstream compartment. An electrical potential difference of about 29 V is applied between the extremities of the cell. At the end of the test (duration Δt: about 48 h here), the specimen is split axially and inner surfaces are sprayed with $AgNO_3$ solution. Once the silver chloride precipitation on the surface is apparent as blue or white shades, as shown in Figure 3, penetration depths can be measured at regular intervals with a caliper since the position of the silver chloride front is clearly identifiable.

Figure 3

The RCMT migration coefficient D_{app}, is given by the following expression:

$$D_{app} = 86.2\frac{TL}{U\Delta t}\left(\overline{x} - 2.088\cdot 10^{-3}\sqrt{86.2\frac{TL\overline{x}}{U}}\right) \quad (1)$$

where D_{app} is also called the chloride ions apparent diffusivity (x10^{-12} m^2.s^{-1}), T is the ambient temperature (K), L is the thickness of the specimen (mm), $\overline{x}$ is the average value of the penetration depth (mm) and U is the potential difference (V) across the sample.

2.4 Resistivity

Measurements were carried out using a Wenner resistivimeter (see description of the Wenner protocol in (Polder 2001)). From the current I (A) and the measured potential difference ΔV (V), the transfer resistance of this quadrupole can be deduced: $R = \Delta V/I$. This quantity depends very strongly on the 3D geometry and inter-electrode spacing a.

To overcome this, it is necessary to standardize it [Marescot et al. 2006] by introducing a geometrical factor *G* which can be calculated with Comsol Multiphysics software. For the geometry considered here, *G* was calculated to be 0.1352 [Palma Lopes et al. 2024].

The apparent resistivity ρ (Ω.m) is then given by the following formula:

$$\rho = G\frac{\Delta V}{I} \tag{2}$$

2.5 Mechanical measurements

In order to determine compressive resistances *Rc*, axial loading was applied on samples (cylindrical specimens, 11 cm diameter and 22 cm height) with a load control system using a hydraulic loading frame with a maximum capacity of 1500 kN. The loading rate was kept constant to a value equal to 2 $kN.s^{-1}$.

Regarding tensile resistances *Rt*, the diametrical loading method (i.e. under the Brazilian test configuration) was used: it provides an estimation of the tensile stress through indirect tension (Djerbi et al. 2008).

The dynamic Young's modulus E_{dyn} was determined using the Impulse Excitation Technique (Grindo Sonic equipment) which is a non-destructive measurement simple to perform [Djerbi et al. 2013]. The Grindo Sonic instrument records the vibration, makes an analysis in the time domain and measures the natural frequency of the dominant vibration mode. The value of E_{dyn} was computed based on the sample dimensions, mass and measured frequency according to ASTM E1876-01 [ASTM, E1876–01, 2001].

3 Experimental results

3.1 Chloride diffusivity

RCMTs were performed after 28 days and 120 days of moist cure. Each time, two tests were carried out per mix design. Fig. 3 shows a tested slice (F40) with the chloride fronts delimited by the orange lines.

Measured D_{app} as a function of the fiber content is shown in Figure 4. The discrepancies between the tests are significant, as variability is inherent to this testing method (Aït-Mokhtar et al. 2013). However, it clearly appears that D_{app} increases with the fiber content: at day 28, from about $2.35 \cdot 10^{-12}$ $m^2.s^{-1}$ (F0) to about $3.6 \cdot 10^{-12}$ $m^2.s^{-1}$ (F60), and at day 120, from about $2.2 \cdot 10^{-12}$ $m^2.s^{-1}$ (F0) to about $3.2 \cdot 10^{-12}$ $m^2.s^{-1}$ (F60). Slight decreases of D_{app} seem to occur between day 28 and day 120 but they are too small to be significant with respect to the measurement uncertainties. Increases of D_{app} are moderate between fiber contents of 0 and 40 $kg.m^{-3}$ and then stronger between fiber contents of 40 and 60 $kg.m^{-3}$. Corrosion affects the fibers from the exposed surfaces to the chloride fronts. In Figure 5a (sample F40), the effects of corrosion on one fiber can be observed in the formation of a preferential pathway for chlorides.

Figure 4

Figure 5

To interpret these observations, it is noteworthy that the potential difference applied during these tests (29 V) inevitably resulted in a decrease in the electrochemical potential of the steel and therefore in a strong acceleration of the corrosion process (Beglarigale and Yazıcı 2017). This phenomenon can be illustrated by the Pourbaix diagram of the Fe-H_2O system (Sousa Rivetti et al. 2017): with a decrease in its potential, the Fe element shifts from the passivity to the corrosion zone. Thus, the increases of D_{app} with fiber content may have been strengthened by this phenomenon.

In (Kim et al. 2021), the authors applied RCMT (using a potential difference of 30 V) to a similar base concrete (50% cement / 50% BFS) at day 28 and found a D_{app} of about $2.5 \cdot 10^{-12}$ $m^2.s^{-1}$ (no fiber) which is similar to the value of $2.35 \cdot 10^{-12}$ $m^2.s^{-1}$ measured here. However, on adding 40 $kg.m^{-3}$ of steel fibers (volume fraction of about 0.5%), they found a decrease of D_{app} by about 30% whereas an increase by about 13% was measured here. Therefore, opposite trends are found between these two studies.

For qualitative observations, a F60 specimen was subjected to natural chloride ingress by immersion in salted water (NaCl: 35 $g.l^{-1}$) during 10 months and then split axially. Figure 5b shows a fiber flush to the exposed face which has been laid bare: some very slight spots of superficial corrosion around the

fibers can be observed to a few millimeters in depth. This adds interesting elements to the above measurements showing that the corrosion process seems in fact to be very slow under natural exposure conditions.

Overall, from these measurements, the optimal fiber content seems to be 40 $kg.m^{-3}$ (volume fraction of about 0.5%): the increase of D_{app} due to the presence of fibers remains quite reasonable up to this fiber content.

3.2 Temporal evolution of resistivity

For the measurements of resistivity, the specimens were tested regularly from day 4 to day 166. Results are shown in Figure 6. For every mix design, a point represents the average value of the measurements performed on several specimens and the error bar represents the standard deviation. Error bars tend to increase with time because the number of available specimens decreased (many tests performed in the framework of the project were destructive), from 13 specimens at day 4 (for every mix design) to only one at day 166 (and hence no error bar).

Figure 6

F0 shows a three-stage evolution: from day 4 to around day 28, resistivity increases fast until it reaches 200 Ω.m. Between day 28 and day 96, resistivity continues to increase but more slowly to reach 276 Ω.m and then, it seems to stabilize to finally reach 287 Ω.m at day 166. This evolution is due to the hydration of the clinker. Over time, the porosity of concrete decreases due to the formation of hydration products. They progressively block the passage of ions, as the interconnectivity between the pores and their size decreases over time.

For mix designs containing fibers, the behavior is similar: a significant increase in resistivity is measured in the first 28 days. At this stage, the concrete is very porous and a large part of the conductivity is induced by the interstitial solution. However, thereafter, the resistivity increases less and finally seems to stabilize. Conductivity is both electrolytic and electronic. As the pores begin to close, conductivity becomes predominantly electronic and is therefore less dependent on the interstitial solution. Obviously, a high dosage of long fibers makes the material highly conductive and

lessens the impact of the characteristics of the pore solution and therefore of the hydration of the material. That being said, for a given content, steel fibers have a constant contribution to the concrete resistivity and presumably do not have any effect on the evolution of the hydration degree.

3.3 Mechanical properties

From mechanical tests performed at day 28, compressive strength *Rc* was found to increase gradually with fiber content, from 54.7 MPa for F0 to 63.5 MPa for F60 (see Table 6). Also, tensile strength *Rt* progressively increases with fiber content, from 5.4 MPa for F0 to 7.1 MPa for F60.

For F40, compared to F0, the increase in tensile / compressive strengths *Rt* and *Rc* are about 26% / 10% respectively at day 28. A fiber content of 60 kg.m^{-3} leads to even better mechanical properties but presents serious disadvantages: a significant increase of D_{app}, and the difficulty of the mixing process despite the addition of superplasticizer. Fiber "urchins" can form, preventing fibers from anchoring in the cementitious matrix (Dinh et al. 2016) and hence propitious to chloride ingress.

Grindosonic measurements performed at day 28 led to a dynamic Young's modulus E_{dyn} of from 47.9 GPa for F0 to 48.3 for F40 and therefore did not evidence a clear effect of the presence of fibers.

4 Modeling by multiscale homogenization methods

4.1 Theoretical background

This section provides an overview of homogenization methods to determine the effective properties of heterogeneous materials. For further developments, see (Buryachenko 2007; Kachanov and Sevostianov 2018).

Here, the property of interest is the local electrical conductivity σ_i in a material phase *i*. The local current density $\mathbf{j}_i$ is expressed as follows:

$$\mathbf{j}_i = \sigma_i \mathbf{e}_i \tag{3}$$

where $\mathbf{e}_i$ is the local electrical field. This is the local expression of Ohm's law. Note that the homogenization of ionic diffusion proceeds by analogy with that of electrical conductivity, by

replacing the local current density by the ionic flux, the electrical conductivity by the diffusion coefficient and the electrical field by the ion concentration gradient.

Considering a Representative Volume Element (RVE) Ω of volume V_Ω in the studied medium, the macroscopic constitutive law is:

$$\mathbf{J} = \boldsymbol{\sigma}^{\text{hom}}\mathbf{E} \tag{4}$$

where $\boldsymbol{\sigma}^{\text{hom}}$ is the homogenized conductivity. This is the classical Ohm's law. **J** and **E** are obtained from volume averages: $\mathbf{J} = \langle \mathbf{j} \rangle_\Omega = \frac{1}{V_\Omega}\int_\Omega \mathbf{j}\,dV = \sum_i f_i \langle \mathbf{j} \rangle_i$ (5)

where: $\langle \mathbf{j} \rangle_i = \frac{1}{V_i}\int_{\Omega_i} \mathbf{j}_i\,dV$, $\langle \mathbf{j} \rangle_i = \frac{1}{V_i}\int_{\Omega_i} \mathbf{j}_i\,dV$, and: $V_\Omega = \sum_i V_i$

$$\mathbf{E} = \langle \mathbf{e} \rangle_\Omega = \frac{1}{V_\Omega}\int_\Omega \mathbf{e}\,dV = \sum_i f_i \langle \mathbf{e} \rangle_i \tag{6}$$

Estimates of the homogenized conductivity are built from a series of auxiliary problems, the so-called Eshelby problems. For each type *i* of heterogeneity with conductivity σ_i, one defines a problem featuring an ellipsoidal inclusion of uniform conductivity σ_i in a uniform reference material with conductivity σ_0, on which an effective uniform electrical field $\mathbf{E}_0$ is applied. Based on Eshelby (1957), the electrical field is uniform inside the ellipsoidal inclusion *i*, with the following expressions:

$$\mathbf{j}_i = \mathbf{A}_0^i \cdot \mathbf{E}_0 \text{ , with: } \mathbf{A}_0^i = \left[\mathbf{I} + \mathbf{P}_0^i \cdot \left(\boldsymbol{\sigma}_i - \boldsymbol{\sigma}_0\right)\right]^{-1} \tag{7}$$

where $\mathbf{I}$ is the identity tensor and $\mathbf{P}_0^i$ is the Hill tensor of the ellipsoidal inclusions *i* which can be expressed as a function of $\boldsymbol{\sigma}_0$ and of the shape of the inclusion.

In the case where the conductivity within the inclusion is not uniform, equation (7) can still be used, provided σ_i is replaced by an equivalent conductivity σ_i^{eff} of the heterogeneous inclusion (Barthélémy and Bignonnet 2020). This will be used in the following to model a fiber surrounded by an interphase as a heterogeneous inclusion. In the case where the inclusion is made of a spheroidal core of

conductivity σ_c surrounded by a spheroidal shell of conductivity σ_s, which is confocal with the core, its equivalent conductivity is obtained by:

$$\boldsymbol{\sigma}_i^{eff} = \boldsymbol{\sigma}_s + \phi_c \left[\left(\boldsymbol{\sigma}_c - \boldsymbol{\sigma}_s \right)^{-1} + \mathbf{P}_s^c - \phi_c \mathbf{P}_s^s \right]^{-1} \quad (8)$$

where ϕ_c is the ratio of the volume of the core to the total volume of the heterogeneous inclusion (core + shell), and $\mathbf{P}_s^c$ (respectively $\mathbf{P}_c^c$) is the Hill tensor of the spheroidal shape of the core (respectively of the whole heterogeneous inclusion) in a reference medium with conductivity $\boldsymbol{\sigma}_s$.

For matrix-inclusion composites, the RVE is now considered as composed of a matrix phase *m* in which are embedded several families of inclusions *i*. In the Mori-Tanaka scheme (Mori and Tanaka 1973), the electrical field localization in each inclusion phase *i* is estimated from the Eshelby problem in which $\boldsymbol{\sigma}_0 = \boldsymbol{\sigma}_m$ and the effective field **e** is taken equal to the intrinsic average of the local electric field over the matrix phase. Then, from the averaging rules (5) and (6), $\boldsymbol{\sigma}^{hom}$ can be estimated by the following expression:

$$\boldsymbol{\sigma}^{\mathrm{hom}} = \left(\sum_i f_i \boldsymbol{\sigma}_i \mathbf{A}_m^i \right) \cdot \left(\sum_i f_i \mathbf{A}_m^i \right)^{-1} \quad (9)$$

This scheme can be used whatever the number *n* of families of ellipsoidal inclusions *i,* each of them being associated with a given ellipsoidal shape, orientation and tensor of electrical conductivity. The family of spheroidal inclusions *i* is defined by its aspect ratio ω_i (axial length / diameter) and by its volume fraction f_i (= V_i/V_Ω) in the RVE. In this work, when the inclusion *i* is not a sphere, an isotropic distribution of orientations of the ellipsoids is assumed (see (Achour et al. 2020), Appendix A for practical details). In the case where the conductivity within the inclusion *i* is not uniform, eq. (9) can still be used, provided $\boldsymbol{\sigma}_i$ is replaced by the equivalent conductivity $\boldsymbol{\sigma}_i^{eff}$ defined in equation (8) (Barthélémy and Bignonnet 2020).

For composites which do not have a matrix phase, the so-called "self-consistent scheme" (Hill 1965) is used instead. Its expression is an explicit equation similar to equation (9), in which $\boldsymbol{\sigma}_m$ is replaced by the sought for $\boldsymbol{\sigma}^{hom}$ and $\mathbf{P}^i_m$ by $\mathbf{P}^i_{\mathrm{hom}}$.

Finally, the resistivity of the homogenized material ρ^{hom} is simply given by $1/\sigma^{hom}$. By analogy, these schemes can be applied to determine the effective chloride diffusivity in the material D_{eff} (Achour et al. 2020).

4.2 The different scales of homogenization

The description of the cement paste is inspired from the multiscale "engineering" models (Pivonka et al. 2004; Pichler and Hellmich 2011; Damrongwiriyanupap et al. 2017). Three main phases are distinguished: anhydrous clinker, hydration products and capillary pores. Moreover, as shown by Figure 7, the description of the cement paste is decomposed in two scales (Achour et al. 2020):

- Level 1: a hydrate foam is described as an aging disordered assemblage of hydration products and capillary pores. To simplify, the hydrates are considered as a single porous phase, which includes gel porosity. Hydrates are modelled by oblate spheroids and the capillary pores by prolate spheroids with a finite aspect ratio, so that the connectivity of these phases will depend on the porosity of the hydrate foam. A self-consistent scheme is used over an isotropic distribution of orientations of both types of spheroids. Aging is accounted for by the reduction of porosity with time obtained from a hydration model.
- Level 2: the cement paste is described as a composite with a matrix of hydrate foam from level 1 in which spherical anhydrous grain inclusions named "clinker" are embedded, using the Mori-Tanaka scheme.

At the scale of mortar (level 3), the Mori-Tanaka scheme is used to represent the mortar with a matrix of cement paste embedding sand particle inclusions, which are considered as spherical.

At the scale of concrete (level 4), the Mori-Tanaka scheme is used. Inside the matrix represented by the mortar, two types of inclusions are considered. Gravels are considered as spherical inclusions. Fibers are considered as prolate spheroidal inclusions. Their distribution of orientation is assumed isotropic. In the case of RCMTs, fibers are assumed surrounded by an interphase. This interphase represents steel which has been completely corroded and assumed as a shell completely devoid of any solid matter. Its equatorial thickness is noted Δr_{int}.

Figure 7

For the different constituents at the different levels, the values of properties, volume fractions and aspect ratios are reported in Table 6. Note that F_h, F_s and F_g are formation factors of the hydrate, sand and gravel phases that will be defined later and VCCTL is the hydration model (see next section).

Table 7

4.3 The hydration model

The Virtual Cement and Concrete Testing Laboratory (VCCTL) software (Bentz and Garboczi 1991; Garboczi and Bentz 1991; Bentz 2005; VTTCL online documentation 2022) was used. It is based on the CEMHYD3D system, widely used in the literature for many cement types and more specifically for Portland and slag blended cements (Chen et al. 2007; Atallah et al. 2023).

Input parameters are the water to cement ratio, the clinker and slag composition and ratios. Outputs include the volume fractions of anhydrous phases, hydration products and capillary pores within the cement paste, the pore solution concentrations for various ions and the resistivity of the pore solution as a function of time: results are shown in Figures 8a and 8b.

Figure 8

The evolutions of the volume fractions are inputs for the homogenization schemes (see e.g., eq. (9)). The pore solution conductivity is input as the conductivity of the capillary pore phase at level 1, and is used to compute the conductivity of the other porous phases (hydrates, sand, gravels, see Table 6).

4.4 Applications

4.4.1 Model input parameters

- Geometrical parameters: the aspect ratio of hydrates ω_h was considered equal to 0.013 (Achour et al. 2020). Based on these authors, the aspect ratio of capillary pores ω_{cp} was considered equal to 6 for CEM I cement pastes, but it is considered here as an adjustment parameter for slag blended cement pastes.

- Volume fractions: at the scale of the paste, the temporal evolution of volume fractions of capillary pores, anhydrous clinker and hydrates was calculated by the hydration model. At the scale of the

mortar, f_p (cement paste) and f_s (sand particles) given in Table 6 are deduced from Table 1. At the scale of the concrete, f_m (mortar) and f_g (gravels) given in Table 6 are deduced from Table 1. For fibers, f_f are between 0 and 0.77% depending on the mix design. Depending on f_f, f_m and f_g were readjusted proportionally.

- Local properties: the temporal evolution of the electrical conductivity of the poral solution in the capillary pores σ_{cp} was calculated by the hydration model. The diffusion coefficient in the interphase, when considered, is set to the one in the capillary pores. The conductivity (and the chloride diffusivity) in the porous phases *i* (hydrates, sand, gravel) is related to the poral solution by their formation factors F_i defined as (Baroghel-Bouny et al. 2011; Chidiac and Shafikhani 2020):

$$\sigma_i = \sigma_{cp} / F_i \quad (10)$$

The formation factors account for the porosity, connectivity and tortuosity of the porous phases. For the aggregates, by assuming that the chloride diffusion coefficient of the aggregates is similarly related to the chloride diffusion coefficient in capillary porosity, it is estimated by: $D_{agg} = D_{cp} / F_{agg}$. From chloride migration tests carried out in (Achour 2018) on a sample of rock coming from the Boulonnais quarry, the formation factor of the sand and gravel is found to be $F_s = F_g = 1.84 \cdot 10^4$. The formation factor of the hydrates F_h was considered as the second adjustment parameter. Electrical conductivity and chloride diffusivity in anhydrous clinker is assumed negligible (see Table 6).

4.4.2 Modeling of temporal evolution of resistivity

The resistivity measurements did not trigger corrosion, hence Δr_{int} is considered equal to 0. Model results and measurements are compared in Figure 9a. Adjustments of ω_{cp} and F_h were performed in such a way that results and measurements are in perfect accordance for the F0 mix design at days 28 and 96: it led to values of ω_{cp} and F_h equal to 8 and $1.25 \cdot 10^4$ respectively. As shown by Fig. 9a, agreement between calculations and measurements is good whatever the fiber content. Most of the numerical results are within the error bars of the measurements. This indicates that the morphological description proposed here is adequate.

Figure 9

From the hydration model, the hydration degrees of clinker and slag at day 166 are 93.5% and 25.3% respectively. Thus, the kinetics of hydration of slag is clearly slower than the kinetics of hydration of the clinker. After day 96, the stabilization of the hydration observed experimentally is only apparent, the hydration of slag continues slowly.

4.4.3 Modeling of chloride diffusivity

The diffusivities D_{app} shown in Fig. 4 are apparent ones. Effective diffusivity D_{eff} (at the scale of the concrete) can be deduced from D_{app} by the following relation (DuraCrete 1998):

$$D_{eff} = \left(\varphi + slp\right) D_{app} \tag{11}$$

where *slp* is the slope of the chloride binding isotherm. According to investigations by Ben Fraj et al. (2012) for a Slag-Based Concrete (SBC) similar to F0, *slp* is estimated at 0.45: this is very close to the value of 0.46 proposed in Reuge et al. (2023). Thus, knowing that φ of the concretes studied here is about 0.11, D_{eff} is approximately equal to $0.56D_{app}$.

From Achour et al. (2018), chloride diffusivity in sand and gravels was measured as $1.1 \cdot 10^{-13}$ $m^2.s^{-1}$. Considering no fiber (F0), model results are shown in Figure 9b: they lead to values of D_{eff} of $3 \cdot 10^{-12}$ $m^2.s^{-1}$ and of $1.95 \cdot 10^{-12}$ $m^2.s^{-1}$ at days 28 and 120 respectively. Such a temporal evolution cannot be really validated by the experimental results due to the measurement uncertainties. From the measurements, at day 120, D_{eff} is $1.23 \cdot 10^{-12}$ $m^2.s^{-1}$: the relative discrepancy of the calculations with the measurements (45%) is rather limited considering the measurement uncertainties and the fact that no adjustment parameter was used here for the model regarding diffusion properties. Moreover, model results (Fig. 9b) show the increase in D_{eff} as a function of the fiber content, considering the three mix designs F20, F40 and F60 and considering Δr_{int} equal to 22 µm. When Δr_{int} = 0 µm, the curves for these fiber contents are superposed on the one for F0. It is noteworthy that from the results of Fig. 9b, the following deduction can be made: if the measurements are not carried out in the same period of time after cast, a decrease of D_{app} can be obtained as a function of the fiber content; this could explain some inconsistent results found in the literature.

In the following developments which focus on the effect of the fiber reinforcement on D_{eff} at day 120, chloride effective diffusivity at the scale of the mortar $D_{Cl,m}$ is adjusted to $2.2 \cdot 10^{-12}$ $m^2.s^{-1}$ to allow a perfect adjustment of D_{eff} with the measurements on the fiber free samples as shown in Figure 10. From Fig. 10, for F20 and F40, adjustment on measurements is good considering Δr_{int} equal to 22 µm. D_{eff} increases almost linearly as a function of the volume fraction of fiber f_f since the latter is very small (below 1%). Experimentally, the trend is also linear for fiber contents between 0 and 40 $kg.m^{-3}$ and then increases further at 60 $kg.m^{-3}$: this may be due to an increasing connectivity of the preferential pathways at such a high fiber content. They develop not only along the corroded fibers but also in the potential crack networks. For F60, Δr_{int} has to be taken equal to 32 µm. Note that Fig. 11 also shows the results obtained with Δr_{int} equal to 0 and 50 µm.

Figure 10

5 Conclusion

SFRBCs with the same base formulation of the concrete (binder: 50% cement, 50% slag) and with four different steel fiber contents, 0 $kg.m^{-3}$ (simple SBC), 20 $kg.m^{-3}$, 40 $kg.m^{-3}$ and 60 $kg.m^{-3}$, were cast and studied. The main conclusions are:

- RCMTs revealed an increase in the chloride ions diffusivity as a function of the fiber content, moderately between 0 $kg.m^{-3}$ and 40 $kg.m^{-3}$ and more significantly between 40 $kg.m^{-3}$ and 60 $kg.m^{-3}$. This is due to the corrosion of the steel fibers induced by the decrease in the electrochemical potential of the steel fibers and by the presence of fiber "urchins" for high fiber content (> 40 $kg.m^{-3}$).

-The optimal fiber content proved to be 40 $kg.m^{-3}$ (corresponding to a volume fraction of about 0.5%) with still a relatively low chloride ions diffusivity and significantly better mechanical strengths than without fibers.

- The temporal evolution of resistivity proved to be slow relatively to OPC based concretes. This is a known effect of the presence of slag which slows down the hydration process. Moreover, as

expected, the presence of steel fibers tends to lower the resistivity of the concrete in proportion to the fiber content. The hydration and resistivity are correlated.

- A multiscale homogenization scheme was developed. In terms of temporal evolution of resistivities, agreement between calculations and measurements was good whatever the fiber content.
- Regarding chloride diffusivities, the model reproduced measurements for fiber contents between 0 and 40 $kg.m^{-3}$ by accounting for the presence of corroded fractions of steel fibers of 22 µm width due to the migration test itself.
- The adequacy of the model with experiments suggests that both the multiscale homogenization scheme and the hydration model are valid and shows the robustness of the approach.

Thus, experimental and modeling points of view are quite complementary and have enabled the mechanisms involved in the case of the SFRSBCs studied here to be identified.

The effects of natural exposure conditions to chloride on the concrete properties remain to be investigated. This would further improve the assessment of the interest of using SFRSBCs for structural purposes in marine environments.

Acknowledgements

This study was carried out within the framework of the WEAMEC program through the B2FE project. WEAMEC and its local partners, Région Pays de la Loire (France), FEDER, CARENE and Nantes Métropole, are gratefully acknowledged for their support. Moreover, progress has been achieved within the framework of the DEMCOM Project (grant ANR-20-CE22-0008-01), funded by the Agence Nationale de la Recherche (ANR). For the purpose of open access, the author has applied a CC-BY public copyright license to any Author Accepted Manuscript (AAM) version arising from this submission.

Declaration of interests

The authors report there are no competing interests to declare.

References

Achour, M. 2018. *Modélisation du couplage carbonatation – chlorures et étude multiéchelle de l'influence des granulats sur la diffusivité dans les bétons*. PhD thesis, Ecole Centrale de Nantes, FR.

Achour, M., Bignonnet, F., Barthélémy, J.-F. et al. 2020. "Multi-scale modeling of the chloride diffusivity and the elasticity of Portland cement paste." *Constr. Build. Mater.*, 234, 117124. https://doi.org/10.1016/j.conbuildmat.2019.117124.

Aït-Mokhtar, A., Belarbi, R., Benboujema, F., et al. 2013. "Experimental investigation of the variability of concrete durability properties." *Cem. Concr. Res.*, 45, 21–36. http://dx.doi.org/10.1016/j.cemconres.2012.11.002.

Ali, B., Farooq, M. A., Kurda, R. et al. 2023. "Effect of type and volume fraction of recycled-tire steel fiber on durability and mechanical properties of concrete" *Eur. J. Environ. Civ. En.*, 27. https://doi.org/10.1080/19648189.2022.2103590.

ASTM E1876-01, Standard Test Method for Dynamic Young's Modulus, Shear Modulus, and Poisson's Ratio by Impulse Excitation of Vibration, ASTM International, West Conshohocken, PA, 2001.

Atallah, J., Ranaivomanana, H., Bignonnet, F. et al. 2023. "A benchmarking of Slag blended cement hydration model. " In *Sciencesconf.org: synercrete 23:423033, SynerCrete'23 - International RILEM conference on synergising expertise towards sustainability and robustness of cement-based materials and concrete structures.* Greece.

Baroghel-Bouny, V., Kinomura, K., Thiery, M. et al. 2011. "Easy assessment of durability indicators for service life prediction or quality control of concretes with high volumes of supplementary cementitious materials." *Cem. Concr. Compos.*, 33(8), 832–847. https://doi.org/10.1016/j.cemconcomp.2011.04.007.

Barthélémy, J.-F. and Bignonnet, F. 2020. "The Eshelby problem of the confocal N-layer spheroid with imperfect interfaces and the notion of equivalent particle in thermal conduction." *Int. J. Eng. Sci.*, 150, 103274. https://doi:10.1016/j.ijengsci.2020.103274.

Beglarigale, A. and Yaz□□, H. 2017. "Electrochemical corrosion monitoring of steel fiber embedded in cement based composites." *Cem. Concr. Compos.*, 83, 427–446. https://doi.org/10.1016/j.cemconcomp.2017.08.004.

Béjaoui, S., Bary, B., Nitsche, S., Chaudanson, D. and Blanc, C. 2006. “Experimental and Modeling Studies of the Link between Microstructure and Effective Diffusivity of Cement Pastes.” *Revue Européenne de Génie Civil* 10 (9): 1073–1106. https://doi:10.1080/17747120.2006.9692906.

Ben Fraj, A., Bonnet, S. and Khelidj, A. 2012. "New approach for coupled chloride/moisture transport in non-saturated concrete with and without slag." *Constr. Build. Mater.*, 35, 761–771. http://dx.doi.org/10.1016/j.conbuildmat.2012.04.106.

Benmokrane, B., Tighiouart, B. and Chaallal, O. 1996. "Bond strength and load distribution of composite GFRP reinforcing bars in concrete." *ACI Mater. J.*, 93(3), 246–253. https://doi.org/10.14359/9810.

Bentz, D. P. and Garboczi, E. J. 1991. "A digitized simulation model for microstructural development." *Ceram. Trans.*, 16, 211–226.

Bentz, D. P. 2005. *CEMHYD3D: A Three-Dimensional Cement Hydration and Microstructure Development Modeling Package: v3.0.* Ed.: NISTIR 7232, Publisher: National Institute of Standards and Technology.

Buryachenko, V. A. 2007. *Micromechanics of Heterogeneous Materials*. Springer New York, NY. https://doi.org/10.1007/978-0-387-68485-7.

Chen, Q., Wang, H., Li, H., Jiang, Z., Zhu, H., Ju J.W. and Yan, Z. 2020. “Multiscale modelling for the ultra-high performance concrete: From hydration kinetics to macroscopic elastic moduli.” *Constr. Build. Mater.*, 247:118541 https://doi.org/10.1016/j.conbuildmat.2020.118541.

Chen, W., Brouwers, H. J. H. and Shui, Z. H. 2007. "Three-dimensional computer modeling of slag cement hydration." *J. Mater. Sci.*, 42, 9595–9610. https://doi.org/10.1007/s10853-007-1977-z.

Chidiac, S. E. and Shafikhani, M. 2020. "Electrical resistivity model for quantifying concrete chloride diffusion coefficient." *Cem. Concr. Compos.*, 113: 103707. https://doi.org/10.1016/j.cemconcomp.2020.103707.

Damrongwiriyanupap, N., Scheiner, S., Pichler, B. et al. 2017. "Self-consistent channel approach for upscaling chloride diffusivity in cement pastes." *Transport Porous Med.*, 118, 495–518. https://doi.org/10.1007/s11242-017-0867-3.

Dinh, N. H., Choi, K. K. and Kim, H. S. 2016. "Mechanical Properties and Modeling of Amorphous Metallic Fiber-Reinforced Concrete in Compression." *Int. J. Concr. Struct. Mater.*, 10, 221–236. https://doi.org/10.1007/s40069-016-0144-9.

Djerby, A., Bonnet S., Khelidj, A. et al. 2008. "Influence of traversing crack on chloride diffusion into concrete" Cem. Concr. Res., 38(6), 877–883. https://doi.org/10.1016/j.cemconres.2007.10.007.

Djerby, A., Bonnet S., Khelidj, A. et al. 20013. "Effect of uniaxial compressive loading on gas permeability and chloride diffusion coefficient of concrete and their relationship." Cem. Concr. Res., 52, 131–139. https://doi.org/10.1016/j.cemconres.2013.05.013.

DuraCrete. 1998. *Modelling of degradation: DuraCrete, probabilistic performance-based durability design of concrete structures*. Ed: European Union.

Eshelby, J. D. 1957. "The determination of the elastic field of an ellipsoidal inclusion and related problems." In *Proceedings of the Royal Society of London. Series A. Math. Phys. Sci.*, 241(1226), 376–396. https://doi.org/10.1098/rspa.1957.0133.

El Achrafi, M.K., Bonnet, S. and Villain, G. 2023. "Electrical resistivity tomography results analyzed with two inversion methods to determine chloride profiles on BFS concrete having very high electrical resistivity." *Constr. Build. Mater.*, **407**: 133361. https://doi.org/10.1016/j.conbuildmat.2023.133361.

Fabien, A., Choinska, M., Bonnet, S. et al. 2022. "Aggregate size effects on the mechanical behaviour and on the gas permeability at damaged state of cement-based materials with and without slag." *Eur. J. Environ. Civ. En.*, 26, 5674–5695. https://doi.org/10.1080/19648189.2021.1915881.

Farooq, S. and Yokota, H. 2022. "Residual mechanical properties of steel fiber reinforced concrete damaged by alkali silica reaction and subsequent sodium chloride exposure." *Ceram. Int.*, 48(17), 24850–24858. https://doi.org/10.1016/j.ceramint.2022.05.138.

Fattouh, M. S., Tayeh, B. A., Agwa, I.S. et al. 2023. "Improvement in the flexural behaviour of road pavement slab concrete containing steel fibre and silica fume." *Case Stud. Constr. Mater.*, 18: e01720. https://doi.org/10.1016/j.cscm.2022.e01720.

Ganesh, G. N. and Sofi, A. J. 2022. "Corrosion Behavior of Fiber-Reinforced Concrete—A Review." Fibers, 10(5): 38. https://doi.org/10.3390/fib10050038.

Hill, R. 1965. "A self-consistent mechanics of composite materials." *J. Mech. Phys. Solids*, 13(4), 213–222. https://doi.org/10.1016/0022-5096(65)90010-4.

Honorio, T., Carasek, H. and Cascudo, O. 2020. "Electrical properties of cement-based materials: Multiscale modeling and quantification of the variability." *Constr. Build. Mater.*, 245: 118461. https://doi.org/10.1016/j.conbuildmat.2020.118461.

Kachanov, M. and Sevostianov, I. 2018. *Micromechanics of materials, with applications*. Springer International Publishing. https://doi.org/10.1007/978-3-319-76204-3.

Kamal, A. S. M. and Boulfiza, M. 2011. "Durability of GFRP Rebars in Simulated Concrete Solutions under Accelerated Aging Conditions." *J. Compos. Constr.*,15(4), 473–481. http://dx.doi.org/10.1061/(ASCE)CC.1943-5614.0000168.

Kim, S., Kim, Y., Usman, M. et al. 2021. "Durability of slag waste incorporated steel fiber-reinforced concrete in marine environment." *J. Build. Eng.*, 33: 101641. https://doi.org/10.1016/j.jobe.2020.101641.

Lawler, J.S., Zampini, D. and Shah, S. P. 2002. "Permeability of cracked hybrid fiber reinforced mortar under load." *ACI Mater. J.*, 99(4), 379–385.

Li, X.-N., Zuo, X.-B., Li, L. and Liu, J.-H. 2024. "Multiscale modeling and simulation on mechanical behavior of fiber reinforced concrete." Int. J. Solids Struct., 286–287:112569. https://doi.org/10.1016/j.ijsolstr.2023.112569

Lu, C., Gao, Y., Cui, Z. et al. 2015. "Experimental Analysis of Chloride Penetration into Concrete Subjected to Drying–Wetting Cycles." *J. Mater. Civ. Eng.*, 27(12): 04015036. https://doi.org/10.1061/(ASCE)MT.1943-5533.0001304.

Marescot, L., Rigobert, S., Palma Lopes, S. et al. 2006. "A general approach for DC apparent resistivity evaluation on arbitrarily shaped 3Dstructures." J. Appl. Geophys., 60(1), 55–67. https://doi.org/10.1016/j.jappgeo.2005.12.003.

Mori, T. and Tanaka, K. 1973. "Average stress in matrix and average elastic energy of materials with misfitting inclusions." Acta Metall., 21(5), 571–574. https://doi.org/10.1016/0001-6160(73)90064-3.

NT Build 492, 1999. *Chloride Migration Coefficient from Non-steady-state Migration Experiments*.

Ortega-Lopez, V., Faleschini, F., Pellegrino, C. et al. 2022. "Validation of slag-binder fiber-reinforced self-compacting concrete with slag aggregate under field conditions: Durability and real strength development." Constr. Build. Mater. 320: 126280. https://doi.org/10.1016/j.conbuildmat.2021.126280.

Pakravan, H. R., Latifi, M. and Jamshidi, M. 2017. "Hybrid short fiber reinforcement system in concrete: A review." *Constr. Build. Mater.*, 142, 280–294. https://doi.org/10.1016/j.conbuildmat.2017.03.059.

Palma Lopes, S., Eid, M.-A., Ibrahim, H. et al. 2023. "Estimation de facteurs géométriques pour des mesures de résistivité avec des géométries de complexité croissante dans le béton." Academic Journal of Civil Engineering, 41(4). https://doi.org/10.26168/ajce.41.4.23.

Pichler, B. and Hellmich, C. 2011. "Upscaling quasi-brittle strength of cement paste and mortar: a multi-scale engineering mechanics model." *Cem. Concr. Res.*, 41(5), 467–476. https://doi.org/10.1016/j.cemconres.2011.01.010.

Pivonka, P., Hellmich, C. and Smith. D. 2004. "Microscopic effects on chloride diffusivity of cement pastes - a scale-transition analysis." *Cem. Concr. Res.*, 34(12), 2251–2260. https://doi.org/10.1016/j.cemconres.2004.04.010.

Polder, R. B. 2001. "Test methods for on site measurement of resistivity of concrete – a RILEM TC-154 technical recommendation." *Constr. Build. Mater.*, 15(2-3), 125–131. https://doi.org/10.1016/S0950-0618(00)00061-1.

Poorsaheli, H.B., Behravan, A. and Tabatabaei Aghda, S. T. 2021. "Durability performance of hybrid reinforced concretes (steel fiber + polyolefin fiber) in a harsh marine tidal zone of Persian Gulf." *Constr. Build. Mater.*, 266: 121176. https://doi.org/10.1016/j.conbuildmat.2020.121176.

Qsymah, A. , Sharma, R. , Yang, Z. , Margetts, L. and Mummery, P. 2017. "Micro X-ray computed tomography image-based two-scale homogenisation of ultra high performance fibre reinforced concrete." *Constr. Build. Mater.* 130, 230–240. http://dx.doi.org/10.1016/j.conbuildmat.2016.09.020.

Rapoport, J., Aldea, C. M., Shah, S. P. et al. 2002. "Permeability of Cracked Steel Fiber-Reinforced Concrete." *J. Mater. Civ. Eng.*, 14(4), 355–358. https://doi.org/10.1061/(ASCE)0899-1561(2002)14:4(355).

Ren, M., Wang, Z., Aoki, H., Takahashi, H. and Maekawa, K. 2024. “Numerical investigation on chloride-induced macro-cell corrosion of steel fiber reinforced concrete.” *Constr. Build. Mater.*, 455: 139194. https://doi.org/10.1016/j.conbuildmat.2024.139194.

Reuge, N., Bignonnet, F. and Bonnet, S. 2023. "Sensitivity analysis of a physicochemical model of chloride ingress into real concrete structures subjected to long-term exposure to tidal cycles. *Appl. Ocean Res.*, 138: 103622. https://doi.org/10.1016/j.apor.2023.103622.

Rezakhani, R., Scott, D. A., Bousikhane, F. et al. 2021. "Influence of steel fiber size, shape, and strength on the quasi-static properties of ultra-high performance concrete: Experimental investigation and numerical modeling." *Constr. Build. Mater.*, 296: 123532. https://doi.org/10.1016/j.conbuildmat.2021.123532.

Shen, L., Di Luzio, G., Cao, M., Ren, Q., Ren, X., Jiang, M., Zhu, D. and Yao, X. 2023. “Insights and theoretical model of thermal conductivity of thermally damaged hybrid steel-fine polypropylene fiber-reinforced concrete.” *Cem. Concr. Compos.*, 138: 105001. https://doi.org/10.1016/j.cemconcomp.2023.105001

Shen, L., Zhang, L., Yang, X., Di Luzio, G., Xu, L., Wang, H. and Cao, M. 2024. "Multiscale cracking pattern-based homogenization model of water permeability in hybrid fiber-reinforced concrete after high-temperature exposure." *J. Build. Eng.*, 84: 108643. https://doi.org/10.1016/j.jobe.2024.108643.

Shin, W. and Yoo, D. Y. 2020. "Influence of steel fibers corroded through multiple microcracks on the tensile behavior of ultra-high-performance concrete." *Constr. Build. Mater.*, 259: 120428. https://doi.org/10.1016/j.conbuildmat.2020.120428.

Song, Z., Li, S. and Yu, Q. 2023. "Chloride induced mechanical degradation of ultra-high performance fiber-reinforced concrete: Insights from corrosion evolution paths" *Constr. Build. Mater.*, 395: 132329. https://doi.org/10.1016/j.conbuildmat.2023.132329.

Sorelli, L., Constantinides, G., Ulm, F.-J. and Toutlemonde, F. 2008. "The nano-mechanical signature of Ultra High Performance Concrete by statistical nanoindentation techniques." *Cem. Concr. Res.*, 38, 1447–1456. http://dx.doi.org/10.1016/j.cemconres.2008.09.002.

Sousa Rivetti, M.L., Neto, J. S. A., de Amorin, N. S. et al. 2017. *Corrosion Inhibitors for Reinforced Concrete. Chapter from Corrosion Inhibitors, Principles and Recent Applications*. Ed. By Mahmood Aliofkhazraei. https://doi.org/10.5772/intechopen.72772.

Stefanoni, M., Angst, U. and Elsener; B. 2015. "Local electrochemistry of reinforcement steel—Distribution of open circuit and pitting potentials on steels with different surface condition." *Corros. Sci.*, 98, 610–618. https://doi.org/10.1016/j.corsci.2015.06.004.

Stora, E., Bary, B. and He, QC. 2008. "On Estimating the Effective Diffusive Properties of Hardened Cement Pastes." Transp. Porous Med., 73, 279–295. https://doi.org/10.1007/s11242-007-9170-z.

Thosmas, J. and Ramaswamy, A. 2007. "Mechanical Properties of Steel Fiber-Reinforced Concrete." *J. Mater. Civ. Eng.*, 19(5): 385–392. https://doi.org/10.1061/(ASCE)0899-1561(2007)19:5(385).

Tsukamoto, M. and Wörner, J.D. 1991. "Permeability of cracked fibre-reinforced concrete." *Darmstadt Concr.: Annu. J. Concr. Concr. Struct.*, 6, 123–135.

Ventura, A., Ta, V. L., Kiessé, T. S. et al. 2020. "Design of concrete: Setting a new basis for improving both durability and environmental performance." *J. Ind. Ecol.*, 25(1), 233–247. https://doi.org/10.1111/jiec.13059.

VCCTL online documentation, 2022. See https://nvlpubs.nist.gov/nistpubs/Legacy/IR/nistir5756.pdf.

XP P18-462 v2, 2017. *Essai accéléré de migration des ions chlorure en régime non-stationnaire*, French national project PERFDUB.

Yang, L., Zhang, Z., Gao, D., et al. 2022. "Mechanical property evolution and chloride transport of steel fiber-reinforced concrete exposed to simulated marine environments." *Mater. Struct.*, 55: 130. https://doi.org/10.1617/s11527-021-01806-7.

Yu, J., Zhang, B., Chen, W., He, J. 2020 " Experimental and multi-scale numerical investigation of ultra-high performance fiber reinforced concrete (UHPFRC) with different coarse aggregate content and fiber volume fraction." *Constr. Build. Mater.*, 260: 120444. https://doi.org/10.1016/j.conbuildmat.2020.120444.

Zhang, Q., Xu, W., Sun, Y. et al. 2022. "Investigation on Mechanical and Microstructure Properties of Steel Fiber Reinforced Concrete." *Adv. Mater. Sci. Eng.*, 2022(1): 3681132. https://doi.org/10.1155/2022/3681132.

Zhao, S., Liu, R. and Liu, J. 2023. "Experimental study of the durability of high-performance cementitious composites with amorphous metallic fibers." *Constr. Build. Mater.*, 367: 130295. https://doi.org/10.1016/j.conbuildmat.2023.130295.

Table 1: Constituents of the base concrete

Constituents	Mass content ($kg.m^{-3}$)	Volume Fraction (%)
Gravels, 12 mm – 24 mm	561.2	21.6
Gravels, 4 mm – 12 mm	432.0	16.7
Sand, ≤ 4 mm	867.8	33.2
Total Aggregates	*1861.0*	*71.5*
CEM I	173.5	5.6
BFS	173.5	6.1
Total Binder	*347.0*	*11.8*
Water	166.6	16.7
Total	*2374.0*	*100*

Table 2: Physical properties of OPC and BFS

Property	OPC	BFS
Specific gravity (g/cm^3)	3.17	2.9
Specific surface area (cm^2/g)	3635	4450
Loss on ignition (950°C)	1.4	< 1.5%
Passing at 32 µm	--	≥ 95%

Table 3: Chemical compounds of OPC and BFS

% of components	OPC	BFS
SiO_2	23.2	34.9
Al_2O_3	3.1	10.9
Fe_2O_3	2.24	0.5
CaO	66.4	42.3
MgO	0.76	6.9
SO_3	2.22	0.1
K_2O	0.18	0.45
Na_2O	0.11	0.35
TiO_2	0.15	0.7

Table 4: Physical properties of steel fibers

Property	Steel fiber
Specific gravity (g/cm^3)	7.8
Length / diameter (-)	70
Resistivity (Ω.m)	$1.43 \cdot 10^{-7}$
Tensile strength (Mpa)	2300
Young Modulus (GPa)	200

Table 5: The four mix designs with different steel fiber contents

Mix design	Fiber content ($kg.m^{-3}$)	Fiber volume fraction (%)	Superplasticizer content ($kg.m^{-3}$)
F0	0	0	2.37
F20	20	0.256	2.44
F40	40	0.513	3.00
F60	60	0.769	3.95

Table 6: Properties of the four mix designs

Mix design	Open porosity at day 28 (%)	*Rc* at day 28 (MPa)	*Rt* at day 28 (MPa)	*Edyn* at day 28 (Gpa)
F0	11.06	54.7	5.4	47.9
F20	11.66	54.8	5.3	46.5
F40	10.98	59.9	6.8	48.1
F60	10.66	63.5	7.1	48.3

Table 7: Input parameters for the multiscale model

Constituent	Electrical conductivity ($\Omega^{-1}.m^{-1}$)	Chloride diffusion coefficient ($m^2.s^{-1}$)	Volume fraction (%)	Aspect ratio (-)
Level 1: Hydrate foam				
Capillary pores	σ_{cp} from VCCTL	$D_{cp} = 2.1 \cdot 10^{-9}$ *	from VCCTL	8 (adjusted)
Hydrate	σ_{cp} / F_h, *with* $F_h = 1.25 \cdot 10^4$ (adjusted)	D_{cp} / F_h	from VCCTL	0.013
Level 2: Cement paste				
Hydrate foam	homog. from level 1	homog. from level 1	from VCCTL	- (matrix)
Clinker	0	0	from VCCTL	1
Level 3: Mortar				
Cement paste	homog. from level 2	homog. from level 2	≈ 46	- (matrix)
Sand	σ_{cp} / F_s	D_{cp} / F_s	≈ 54	1
Level 4: Concrete				
Mortar	homog. from level 3	homog. from level 3 or adjusted to $2.2 \cdot 10^{-12}$	62	- (matrix)
Gravels	σ_{cp} / F_g, with $F_g = F_s$	D_{cp} / F_g	38	1
Steel fiber with interphase	steel core: 7.10^6 no interphase ($\Delta r_{int} = 0$)	steel core: 0 interphase: D_{cp}	between 0 and 0.77	equivalent inclusion: 70 steel core: depending on Δr_{int}

*Cl ions diffusivity in free water

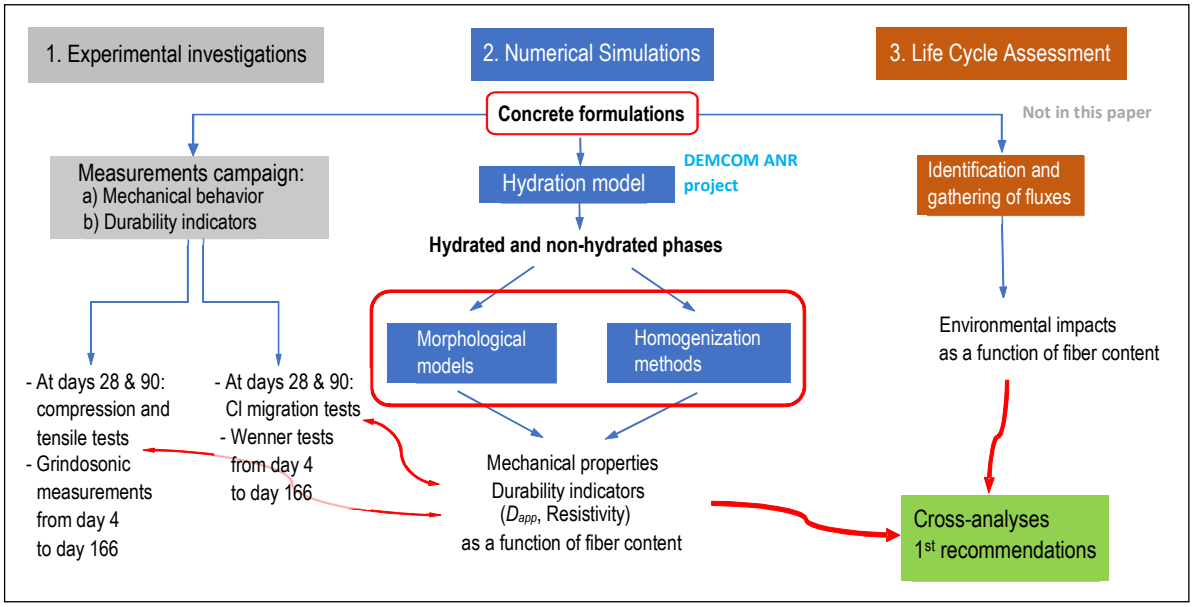

Figure 1

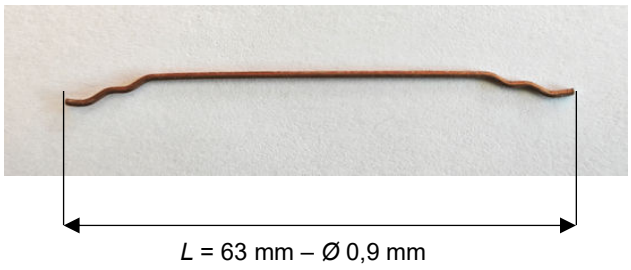

Figure 2

Figure 3

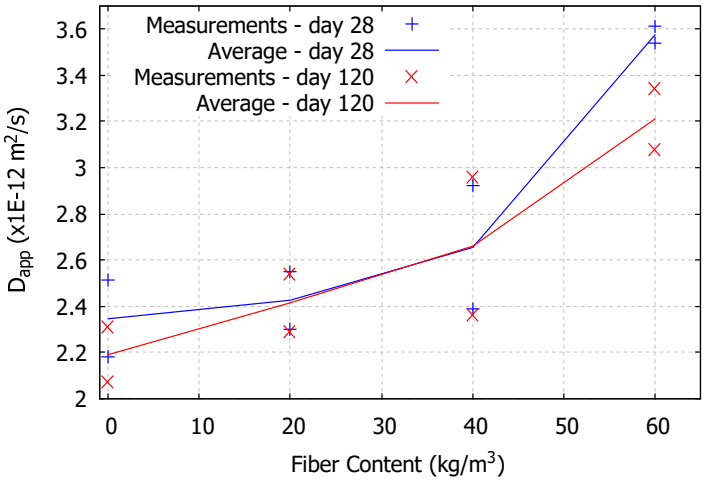

Figure 4

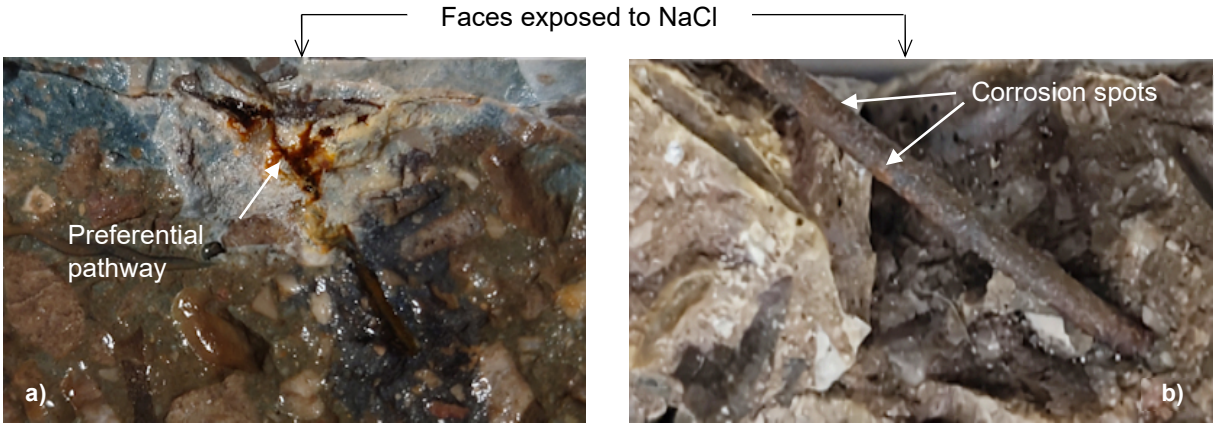

Figure 5

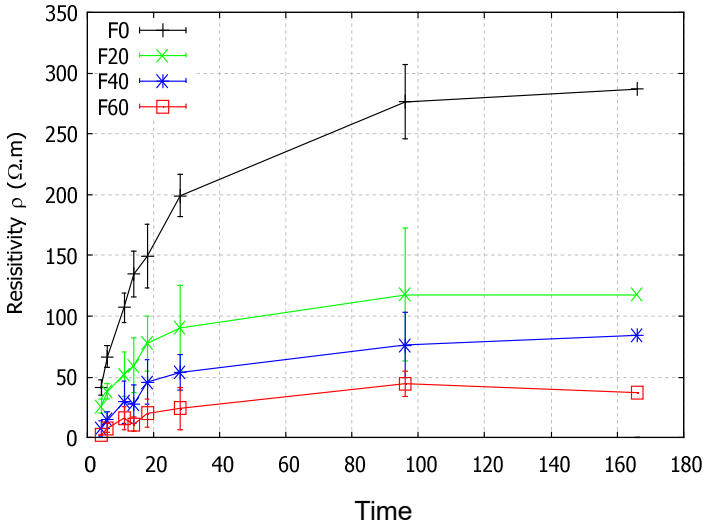

Figure 6

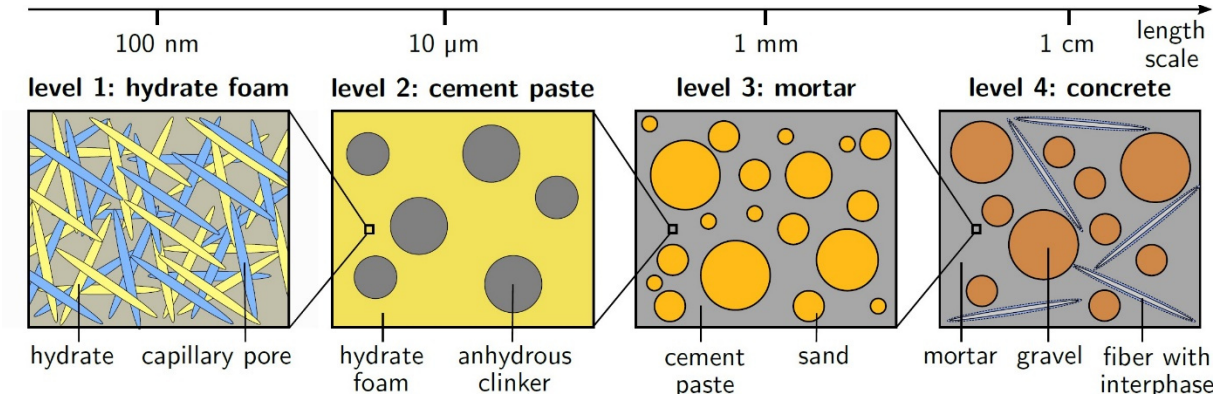

Figure 7

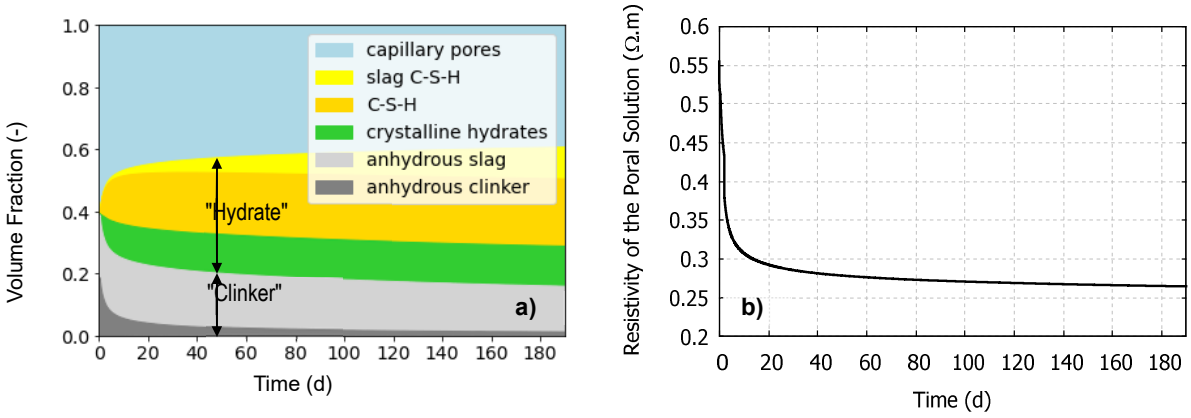

Figure 8

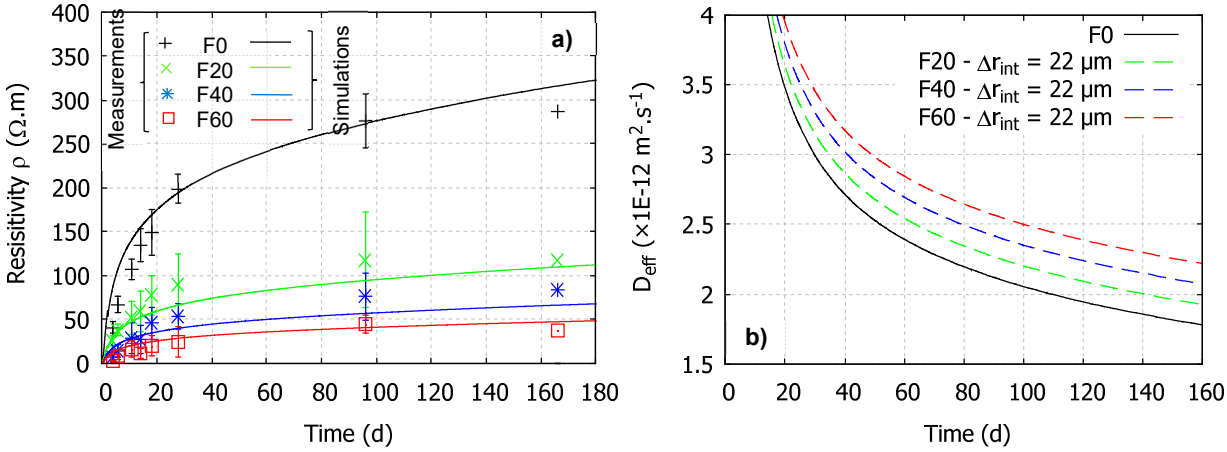

Figure 9 (9a,9b)

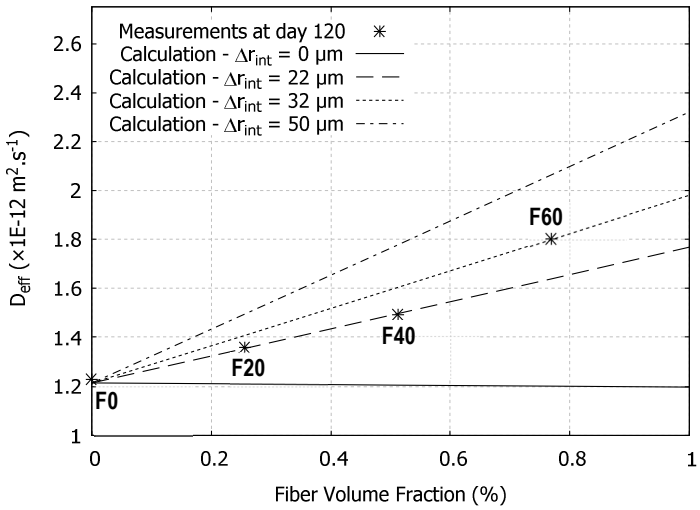
Measurements at day 120
Calculation - Δr_int = 0 µm
Calculation - Δr_int = 22 µm
Calculation - Δr_int = 32 µm
Calculation - Δr_int = 50 µm
D_eff (×1E-12 m².s⁻¹)
Fiber Volume Fraction (%)
F0
F20
F40
F60
2.6
2.4
2.2
2
1.8
1.6
1.4
1.2
1
0
0.2
0.4
0.6
0.8
1

Figure 10

Figure captions

Figure 1. Schematic diagram of the project

Figure 2. Double-hooked steel fiber, "Dramix 5D" from Bekaert™

Figure 3. F40 sample split after RCMT, chloride fronts delimited by the orange lines

Figure 4. Apparent chloride diffusivities measured by RCMTs at day 28 and day 120 as a function of the fiber content

Figure 5. (a) Preferential pathway formed by the total corrosion of a steel fiber (F40 sample split) after RCMT, (b) macrophotograph of an exposed steel fiber after natural conditions of chloride ingress (F60 sample split)

Figure 6. Temporal evolution of concrete resistivity measured for the four mix designs

Figure 7. The four levels of homogenization, from the hydrate foam to the concrete

Figure 8. Results of the hydration model as a function of time, (a) volume fractions of the different phases and (b) resistivity of the poral solution

Figure 9. Temporal evolutions of (a) concrete resistivity, measurements (points) and numerical simulations (curves) and (b) effective chloride diffusivity obtained by the numerical simulations, for the four mix designs

Figure 10. Effective chloride diffusivities as a function of the fiber content at day 120, measured by RCMTs (points) and obtained by the numerical simulations (lines)